De novo design of a biologically active amyloid

Rodrigo Gallardo[1,2], Meine Ramakers[1,2], Frederik De Smet[1,2], Filip Claes[1,2], Ladan Khodaparast[1,2,3], Laleh Khodaparast[1,2,3], José R. Couceiro[1,2], Tobias Langenberg[1,2], Maxime Siemons[1,2,4], Sofie Nyström[5], Laurence J. Young[6], Romain F. Laine[6], Lydia Young[7,8], Enrico Radaelli[9,10], Iryna Benilova[9,10], Manoj Kumar[11], An Staes[12,13], Matyas Desager[1,2,4], Manu Beerens[14], Petra Vandervoort[14], Aernout Luttun[14], Kris Gevaert[12,13], Guy Bormans[4], Mieke Dewerchin[15,16], Johan Van Eldere[3], Peter Carmeliet[15,16], Greetje Vande Velde[17], Catherine Verfaillie[11], Clemens F. Kaminski[6], Bart De Strooper[9,10], Per Hammarström[5], K. Peter R. Nilsson[5], Louise Serpell[18], Joost Schymkowitz[1,2,*] & Frederic Rousseau[1,2,*]

[1] VIB Switch Laboratory, Leuven, Belgium

[2] Department for Cellular and Molecular Medicine, KU Leuven, Belgium

[3] Laboratory of Clinical Bacteriology and Mycology, Department of Microbiology & Immunology, KULeuven, Belgium.

[4] Laboratory of Radiopharmacy, Department of pharmaceutical and pharmacological sciences, KU Leuven, Belgium

[5] IFM Department of Chemistry, Linköping University, Linköping, Sweden.

[6] Department of Chemical Engineering and Biotechnology, University of Cambridge, New Museums Site, Pembroke Street, Cambridge CB2 3RA, UK.

[7] Astbury centre for Structural Molecular biology, university of leeds, leeds, UK.

[8] School of Molecular and cellular biology, university of leeds, leeds, UK.

[9] VIB Center for the Biology of Disease, 3000 Leuven, Belgium

[10] Center for Human Genetics and Leuven Institute for Neurodegenerative Diseases (LIND), University of Leuven, 3000 Leuven, Belgium

[11] Stem Cell Institute, University of Leuven (KU Leuven), Leuven, Belgium

[12] VIB Medical Biotechnology Center, VIB, Ghent, Belgium.

[13] Department of Biochemistry, Ghent University, Ghent, Belgium.

[14] Department of Cardiovascular Sciences, Center for Molecular and Vascular Biology Research Unit, Endothelial Cell Biology Unit, KU Leuven, B-3000 Leuven, Belgium

[15] Laboratory of Angiogenesis and Vascular Metabolism, Department of Oncology,, KULeuven B-3000, Belgium

[16] Laboratory of Angiogenesis and Vascular Metabolism, Vesalius Research Center, VIB, Leuven B-3000, Belgium

[17] Biomedical MRI Unit/MoSAIC, Department of Imaging and Pathology, KU Leuven, Leuven, Belgium

[18] School of Life Sciences, University of Sussex, Falmer, East Sussex BN1 9QG, U.K

* to whom correspondence should be addressed: frederic.rousseau@switch.vib-kuleuven.be or joost.schymkowitz@switch.vib-kuleuven.be

ABSTRACT

Most human proteins possess amyloidogenic segments, but only about 30 are associated to amyloid-associated pathologies and it remains unclear what determines amyloid toxicity. We here designed vascin, a synthetic amyloid peptide, based on an amyloidogenic fragment of VEGFR2, a protein that is not associated to amyloidosis. Vascin recapitulates key biophysical and biochemical characteristics of natural amyloids, penetrates cells and seeds the aggregation of VEGFR2 by direct interaction. We find that amyloid toxicity is observed only in cells that both express VEGFR2 and are dependent on VEGFR2 activity for survival. Thus amyloid toxicity here appears to be both protein specific and conditional, *i.e.* determined by VEGFR2 loss-of-function in a biological context where target protein function is essential.

INTRODUCTION

Amyloid aggregation of proteins is driven by short amyloidogenic sequence segments within a protein chain (*1, 2*) that have the potential to self-assemble into β-sheet ribbons to form the characteristic cross-beta structured spine of amyloid structures (*3, 4*). It has been shown that most proteins do in fact possess such amyloidogenic sequence segments (*5, 6*). Still, only about 30 human proteins are known to be involved in amyloid-associated diseases (*7, 8*). Moreover it is still not clear what determines amyloid toxicity in these diseases (*8, 9*). Here we investigate whether an endogenously expressed protein that possesses amyloidogenic potential but aggregates neither under normal nor pathological conditions, can be induced to do so by seeding with a peptide consisting of an amyloidogenic fragment of its own sequence. The use of amyloidogenic fragment peptides is motivated by the observation that aggregation of disease–associated amyloidogenic proteins can be seeded by such peptides *in vitro* (*10, 11*) and that truncations of amyloid proteins have been associated with increased seeding potential *in vivo* (*12, 13*). Moreover it has been shown that amyloidogenic peptides and proteins are generally much more efficient at seeding aggregation of homotypic sequences (*14-16*) although examples of cross seeding do exist (*17-19*). Indeed, seeding of protein aggregation *in vitro* appears to work universally, and fits with the structural model of aggregation as the addition of new strands to a growing amyloid fibril (*8*). This imparts sequence

specificity to the seeding process as the incorporation of non-homologous sequences into the highly ordered in-register stacking of identical side chains in the fibril core is likely to be energetically disfavoured (*13, 20, 21*). The seeding concept appears to hold true both in cell culture and *in vivo*, even for non-prion aggregation-associated peptides and proteins, which have hence been called prionoids (*22*). As a target protein we choose VEGFR2 as the function of this protein is well characterized. To ensure efficient seeding we designed an amyloidogenic peptide termed vascin consisting of a tandem repeat of an amyloidogenic sequence segment in the VEGFR2 signal peptide.

We find that vascin is a *bona fide* amyloidogenic peptide that forms mature cross-beta fibrils along with prefibrillar intermediates including soluble oligomers and protofibrils. Moreover we find that the peptide is able to enter cells and reach the cytoplasmic compartment and specifically induce the aggregation of endogenous VEGFR2 thereby inhibiting its function in Human Umbilical Vein Endothelial Cells (HUVEC) *in vitro* and reducing VEGFR2-dependent tumor progression *in vivo*.

It remains unclear what determines amyloid toxicity in amyloid diseases and whether cell death results from a consequence of direct amyloid toxicity (gain-of-function) or whether it is a consequence of loss-of-function (*23, 24*). However, our detailed understanding of real amyloid disease models is often insufficient to address these questions directly. Indeed for many disease associated amyloidogenic proteins –such as the Aβ peptide in Alzheimer disease (*25*) and α-synuclein in Parkinson disease (*26*)- we still have insufficient understanding both of their physiological role as well as the cellular interactions of the amyloid conformation in disease (*26, 27*). We do however have a better understanding of the structural and biochemical characteristics that are common to most amyloid diseases. These features include the cross-beta structural organization of the spine of the amyloid fibrils formed by short segments of the sequence, the population of prefibrillar intermediates including soluble oligomers and protofibrils, and the capacity of amyloids to seed aggregation of the native conformation. While our artificial amyloid model recapitulates these key structural and biochemical features of natural amyloids, it is also simple enough to investigate the relationship between protein loss-of-function and amyloid toxicity.

Our results show that vascin amyloids are not inherently toxic but that the emergence of amyloid toxicity is dependent on biological context. Vascin is not toxic

to cells that do not express VEGFR2 or to cells expressing VEGFR2 but that are not dependent on VEGFR2 function. However when introduced in VEGFR2 dependent cells we find association of vascin amyloid toxicity and VEGFR2 loss-of-function. Our model system therefore demonstrates that amyloidogenic protein fragments can induce aggregation of non amyloidogenic proteins and that under these conditions amyloid gain of function is a phenotypic effect resulting from cell context specific loss-of-function.

RESULTS

Design of vascin, an amyloidogenic peptide derived from a VEGFR2 fragment

We analyzed the VEGFR2 proteins from mouse and human using the statistical thermodynamics algorithm TANGO (*28*) (Figure S1A). Since we envisaged testing the sequence ultimately in a mouse model, we opted for maximal compatibility with the murine protein. Moreover, the two homologs share 84% sequence identity overall and 90% in the TANGO-regions. To derive peptide sequences that are likely to form amyloid structure in isolation, but also have a high potential for forming soluble oligomers (*29*), we devised a strategy (*30, 31*) that makes use of a sequence feature of functional amyloids and yeast prions, which often contain several Aggregation Prone Regions (APR) (*32*) closely connected by disordered regions (*33*). Hence we placed two APRs in a peptide, separated by a rigid proline-proline linker, mimicking these repeat patterns. In order to maintain colloidal stability and solubility of the sequence, we supercharged the peptides by flanking the APRs with either negatively charged aspartate or positively charged arginine residues. Given the length limitations imposed by the efficiency of solid phase peptide synthesis, this design scheme imposes a length limitation on the APRs of 7 amino acids. Hence we selected 10 such high scoring sequences (Table S1) and generated the 38 peptide sequences listed in Supplementary Table 2, which explore both tandem repeats of the same APR as well as fusions of different APRs. Peptides were screened for their ability to inhibit VEGF signaling in HEK293 cells transfected with mouse VEGFR2. To this end, cells were treated overnight with an apparent concentration of 20 μM peptide (assuming 100% synthesis efficiency) and ERK phosphorylation was determined after stimulation for 5 min with 25 ng/mL VEGF (Figure S1B). At this concentration, we observed inhibition only with 2 peptides (B8 and B12). The effect was most

pronounced with the peptide B8, which was based on a tandem repeat of the first high scoring aggregation prone region in the sequence that belongs to the signal peptide and has the sequence $L_6AVALWF_{12}$ (Figure S2A), resulting in the sequence DLAVALWFDPPDLAVALWFD (pI = 3.38, M.W. = 2272.15 Da). We termed this peptide vascin (Figure S2B), obtained additional material by solid phase peptide synthesis followed by HPLC purification (Figure S2C), and confirmed its identity by mass spectrometry (observed mass: 2272.4, Figure S2D).

Vascin forms soluble β-structured oligomers that mature into amyloid fibrils

To determine the amyloidogenic nature of the peptide, vascin was dissolved to a final concentration of 300 μM in 1% (w/v) ammonium bicarbonate in ddH_2O. After 24 hours incubation Transmission Electron Microscopy (TEM) revealed typical amyloid fibrils of about 10 nm in width consisting of protofilaments of 4-5 nm (Figure 1A-D and Figure S3). Additionally, vascin fibrils bind amyloid sensor dyes, including Thioflavin-T and the amyloid specific oligothiophene h-HTAA (34) (Figure 1E). X-ray diffraction of aligned bundles of vascin fibrils confirmed their cross-beta nature, with characteristic diffractions at 4.7 and 10Å (Figure 1F). Together these data confirm the amyloidogenic nature of vascin. In order to follow amyloid formation kinetics we filtered 100 μM dissolved vascin 1% (w/v) ammonium bicarbonate in ddH_2O through a 0.2 μm regenerated cellulose filter and monitored particle size distribution using electrospray ionisation-mass spectrometry linked to ion mobility spectrometry (ESI-IMS-MS)(35) (Figure 1G) and Dynamic Light Scattering (DLS) (Figure 1H). At time zero, the MS resolved a mixture of monomers and multimers up to heptamers (Figure 1G), whereas the particle sizes estimated through DLS ranged from 5-100 nm (assuming linear polymer particles). This indicates that the filtered vascin solution contains soluble oligomeric aggregates already at time zero. After 6 h particles reached sizes over 1 μm (Figure 1H). The fact that no lag phase was observed in the evolution of the DLS autocorrelation function (Figures S4A & B) further suggests that these soluble oligomers are able to directly proceed to amyloid fibril formation. In order to probe the secondary structure of these soluble aggregates we monitored the same aggregation kinetics using Fourier Transform Infra-Red spectroscopy (FT-IR). The spectrum at time zero was dominated by maxima near 1630 and 1690 cm^{-1} (Figure 1I), characteristic of β-sheet

structure. Over the following 3h the intensity of these peaks increased markedly while the center of the peaks shifted gradually to 1622 and 1692 cm^{-1}, respectively (Figure 1I&J). These peaks were quite narrow and regions outside the peaks showed very little absorption, suggesting that most of the peptide sequence is involved in β-structured hydrogen bonding. FT-IR kinetics therefore indicate that vascin largely adopts a β-structured conformation upon solubilization in 1% ammonium bicarbonate and that these species mature into amyloid fibrils over time. Finally, we measured binding to 8-anilino-1-naphthalenesulphonic acid (ANS) during vascin amyloid formation (Figure S4C), revealing high binding of this dye at time zero. The latter is a typical feature of interaction-prone cytotoxic prefibrillar oligomers that present a high degree of solvent exposed hydrophobic surface (*36*). The binding of ANS increased over time, suggesting hydrophobic surfaces stay exposed upon fibril formation. We also verified the amyloidotypic double peak fluorescence spectrum of vascin with the LCO hHTAA in contrast to the scrambled peptide (Figure S4D). Given that the above observations were made at 300 μM peptide where the signal to noise ratio for biophysical characterisation is optimal, we also verified that vascin readily formed amyloid fibrils at the lower concentration of 30 μM (Figure S5). Compared to vascin a scrambled version of the peptide (Note S1) formed small soluble aggregates with hydrodynamic radii smaller than 100 nm as estimated by DLS (Figure S6A&B) that exhibited a non-fibrillar morphology via TEM (Figure S6C), and displayed marginal affinity for the amyloid sensor dyes with no specific emission spectrum for amyloid fibers (Figure 1E and S4D). Similar observations were made with a vascin variant in which proline mutations were introduced to break the beta-sheet propensity of the APRs in vascin (Note S2 and Figure S7). In contrast, a version of vascin based on the human sequence (h. vascin, DLAVALWLDPPDLAVALWLD), containing a single mutation of phenylalanine to leucine at position 7 of the APR, displayed similar amyloid formation as the original mouse sequence (Figure S8).

In conclusion the biophysical characterization above confirms that vascin is an amyloidogenic peptide that readily forms β-structured soluble oligomeric aggregates that mature into cross-β structured amyloid fibrils in a broad concentration range.

Vascin inactivates VEGFR2 in HUVEC cells by specifically inducing its aggregation

As vascin is an amyloidogenic peptide derived from a VEGFR2 fragment we investigated whether it displays biological activity towards VEGFR2 in cultured cells. First, we monitored cellular uptake of vascin using carboxyfluorescein labelled vascin (CF-vascin) in HUVEC cells. We observed cellular uptake during the first hour of incubation as small vesicles or inclusions that contained diffuse homogeneous peptide (Figure 2A). Moreover, these inclusions were positive for the amyloid sensor dye pFTAA (Figure 2B&C), showing that the peptide remains in an amyloid-like conformation inside the cells. Co-staining for the ER protein Calnexin reveals that the peptides are on the cytoplasmic side of the ER (Figure 2D), where they partially overlaps with staining for ribosomes (Figure 2E). Proximity ligation (Duo-Link) using antibodies against VEGFR2 and the carboxyfluorescein-label on vascin (Figure 2F), quantified by image analysis from high content microscopy demonstrated direct interaction between vascin and VEGFR2 (Figure 2G). This result was further confirmed by two color direct stochastic optical reconstruction microscopy (dSTORM) super-resolution imaging(37) using 0.5μM of Alexa647 labeled vascin and Alexa568 labeled immunodetection of VEGFR2 (Figure 2H&I).

Co-immunoprecipitation of VEGFR2 from lysates of vascin-treated HUVECs was performed with PEG-biotin labeled peptide again demonstrating direct interaction between vascin and VEGFR2 (Figure 3A). To investigate the consequences of the interaction between vascin and VEGFR2 on the aggregation status of the receptor, we determined the difference in distribution of VEGFR2 between soluble and insoluble fractions of lysates from HUVECs treated with 20 μM of vascin. Upon vascin treatment we could observe a clear redistribution of full length and partially degraded VEGFR2 towards the insoluble fraction whereas this was not the case upon treatment with scrambled vascin (Figure 3B). In addition, the induced insoluble VEGFR2 displays partial resistance to the ionic detergent SDS, a hallmark of amyloid-like aggregation (Figure 3C). To confirm that vascin mediated aggregation of VEGFR2 in HUVECs leads to its loss-of-function we determined the dose response curve of vascin on VEGFR2 autophosphorylation and ERK phosphorylation (MSD ELISA assay) after stimulating HUVECs for 5 min with 1.3 nM VEGF. HUVECs displayed a clear dose responsive inhibition by vascin with an IC50 of 6.8 ± 0.5 μM for receptor autophosphorylation and 8.3 ± 0.4 μM for ERK phosphorylation (Figure 3D&E). The human version of vascin showed similar

inhibition, which was not observed using the scrambled or proline controls (Figure 3F). Using fluorescence-activated cell sorting (FACS) we observed a concomitant reduction in the surface expression of VEGFR2 in HUVECs, but not of the unrelated cell-surface protein CD29 (Figure 3G & Figure S9), confirming loss of VEGFR2 function in HUVECs. Together these data show that vascin is internalized by HUVECs and reaches the cytoplasmic compartment where it directly binds to VEGFR2 and localizes with ribosomes, resulting in the functional inactivation through aggregation of VEGFR2. This effect seemed to be specific as indicated by the CD29 result. Moreover, we observed no effect of vascin on EGF signalling in HeLa cells, which do not endogenously express VEGFR2 but the functionally homologous EGFR. Threatment of this cell line with 20 μM vascin showed no inhibition of ERK phosphorylation when stimulated with EGF (Figure 3H), showing that the inhibitory effect of vascin on ERK phosphorylation is specific for VEGFR2 stimulation. To test if known amyloidogenic proteins were affected by vascin, we investigated the effect of adding vascin to solutions of the Alzheimer β-peptide 1-42 (Aβ, Figure 3I) or the human Prion protein (PrP, Figure 3J) and monitored aggregation through ThT fluorescence emission. The mean lag time for unseeded aggregation of Aβ1-40 was 350 minutes whereas addition of preformed Aβ fibrils decreased the lag time to 130 minutes. Addition of vascin fibril variants did not lead to significant decrease of fibrillation lag times other than for scrambled vascin where the significance level in a paired T-test was $p > 0.03$. The mean lag time for spontaneous conversion of HuPrP23-231 was 1100 minutes. The conversion rate upon addition of preformed HuPrP90-231 fibrils was shortened to 135 minutes whereas addition of preformed vascin fibril variants did not lead to significant alteration of lag time. These data demonstrate that no vascin cross-seeding occur for these proteins.

Vascin reduces VEGFR2-dependent tumor growth in mice

To establish the effect of vascin *in vivo* we turned to a functional angiogenesis model that is sensitive to inhibition of VEGFR2 *in vivo* and used a subcutaneous B16 melanoma syngenic tumor model in C57BL/6 inbred mice. Tumor growth of this line is strongly reduced by VEGFR2-specific inhibition approaches, such as the tyrosine kinase inhibitor PTK 787/ZK 222584 (*38*), providing a sensitive phenotypic readout for the anticipated effect of vascin. To assess if vascin administration would be

tolerated by C57BL/6 mice we first performed a dose-escalation study by daily intravenous (iv) tail vein injection in two six-week-old, inbred C57BL/6 mice, starting from 1 mg/kg to 10 mg/kg biotin-PEG vascin, which corresponded to the highest stock concentration of the peptide that we could reach with the available material. No adverse effects to the basic physiological and behavioral parameters of the animals were apparent across this concentration range, including body weight, food and water consumption, home cage activity and locomotion. To test the effect of vascin on tumor growth, B16 cells were injected subcutaneously in the right dorsal flank of eight-week-old C57BL/6 mice. Starting from three days post tumor injection and until day 17, mice were treated daily by iv injection of 10 mg/kg biotin-PEG vascin (N=10) or scrambled vascin as the negative control (N=10). Another negative control group received iv injection of the vehicle (50 mM Tris HCl pH7.5, N=10) and the positive control group (N=5) received the kinase inhibitor PTK787 orally (75mg/kg). Tumor growth was similar in animals treated with scrambled vascin or vehicle, and markedly reduced in animals that received the PTK inhibitor. In the vascin treated group tumor growth was significantly inhibited compared to the negative controls over the entire experiment (ANOVA with Tukey post-hoc) and up to day 14 to a similar extent as the PTK treated group (Figure 4A).

In order to exclude overall toxicity effects of vascin on the general physiology of the mouse, we executed a short term toxicology study in which we treated groups of 5 mice daily with iv injections of vascin (10 mg/kg, group A), scrambled (10 mg/kg, group B) or vehicle (50 mM Tris pH 7.5) for 14 days (the same duration as the tumor growth experiment). Gross examination at necropsy did not reveal any macroscopic changes (Figure S10A). Concerning organ weights (Figure S10B), hematology (Figure S10C) and clinical chemistry (Figure S10D), no statistically significant differences were observed among groups. Also no significant variations were observed among the experimental groups in terms of lesion spectrum, frequency and severity. In addition, we examined brain sections from all the animals for amyloid deposition and associated astrogliosis. Thioflavin-S-positive deposits in the brain parenchyma were not detected (Figure S11 A, B & C) and co-staining with GFAP (glial fibrillary acidic protein) did not show any morphological evidence of astrogliosis, in sharp contrast to the positive control (Figure S11D), for which we employed a transgenic Alzheimer

disease mouse model that has marked amyloid deposition throughout the cortex and hippocampus (*39*).

In order to demonstrate the arrival and presence of vascin at the tumor site, two groups of tumor-bearing mice were injected iv with 10 mg/kg CF-vascin or vehicle (50mM Tris HCl pH 7.5, negative control) and imaged with whole-body fluorescence imaging. Because the melanin-expression by the tumors strongly absorbs light hampering the *in vivo* detection of fluorescence, tumors were isolated 30 min after injection and imaged *ex vivo*. The resulting fluorescence images showed strong green fluorescence emission for tumors isolated from CF-vascin-injected mice, whereas no fluorescence could be detected from tumors isolated from vehicle-injected control mice (Figure S12A), supporting the presence of vascin-CF at the tumor site based on macroscopic CF-fluorescence measurements. To further verify the presence of CF-vascin inside the tumor tissue with microscopic resolution, we additionally examined the presence of CF-vascin with Fibered Confocal Fluorescence Microscopy (FCFM) on tumor samples from the same mice. Inserting the fibre-optical probe inside the tumor tissue sample of vehicle-injected control mice did not show any fluorescence signal, whereas the tumor samples of CF-vascin-injected mice were clearly positive for green fluorescence (Figure S12B). To quantify vascin in B16 tumors, the specific light absorption by melanomas was calibrated through the addition of different known quantities of CF-vascin to series of tumor tissue dilutions and compared to a standard curve of fluorescence intensity for a dilution series of pure CF-vascin. Both were found to be linear in a large concentration range and for two different fluorescence imaging modalities, thereby cross-validating the results (Figure S13A&B). The tumor-specific fluorescence attenuation was then used to estimate the concentration of CF-vascin in tumors isolated from CF-vascin-treated mice, which was established to be 26.4 ± 10.5 µM, a concentration that is well above the IC50.

Taken together these data are consistent with a direct inhibitory activity of vascin on VEGFR2 function *in vivo* in the same manner that was observed in cells.

Amyloid toxicity is conditional to VEGFR2 dependence of cells

We determined loss of VEGFR2 function and vascin amyloid toxicity in several cell lines. CellTiter-Blue cytotoxicity assays (Figure 4B) revealed that in HUVECs loss

of function of the receptor (IC_{50} of 6.8 ± 0.5 μM for receptor autophosphorylation and 8.3 ± 0.4 μM for ERK phosphorylation) goes hand in hand with cytotoxicity. On the other hand in HEK293 or U2OS cells neither 2.5-100 μM of vascin or its scrambled counterpart were found to be toxic (Figure 4C&D). Upon transfection of VEGFR2 in HEK293 we observed that, after VEGF stimulation, ERK phosphorylation was inhibited upon treatment with 20 μM vascin (Figure S14A) which induced the aggregation of the VEGFR2 as evidenced on the fractionation assay (Figure S14B). However, no noticeable toxicity of vascin to HEK293 cells expressing VEGFR2 was observed in the range of 2.5 - 100 μM (Figure 4E). This demonstrates that vascin is not toxic to HEK293 cells in the absence of VEGFR2 but also that aggregation of transiently expressed VEGFR2 in these lines does not affect cell viability. Similar observations were made with U2OS cells expressing VEGFR2 (Figure 4F). Thus vascin does not display generic amyloid toxicity and the aggregation of VEGFR2 by vascin is in itself also not toxic. Finally, as neurons are particularly sensitive to aggregate toxicity we assessed the toxicity of vascin to primary cortical neurons, which do not express VEGFR2. Although with these neurons we observed significant toxicity upon peptide treatment (Figure 4G), CellTiter-Blue reaction levels were similar for the vascin and its scrambled non-amyloid variant, suggesting that the toxicity was not amyloid-specific but rather reflects the high sensitivity of these cultures, which also resulted in a large variability in the assay. To verify this further we turned to human iPSCs differentiated to a cortical neuronal phenotype, which was verified using q-RT-PCR and immunostaining for markers specific for this cell type (Figure S15). In these cultures we observed a lack of amyloid-specific toxicity, although there is 10% toxicity associated with administration of both vascin or the scrambled control (Figure 4H).

Together these data suggest that amyloid toxicity is not dependent on cell type or even on target protein aggregation but that amyloid toxicity is mainly determined by the biological context in which the target protein is inactivated by aggregation. As HUVEC survival is dependent on VEFGR2 function, its molecular loss of function by aggregation translates in gain of toxic phenotype.

DISCUSSION

About thirty amyloidogenic proteins are known to contribute to human disease. These diseases include neurodegenerative diseases such as Alzheimer's or Parkinson's disease but also organ-specific and systemic amyloidosis such as diabetes mellitus type-2 or light chain amyloidosis(*7*). Although the pathophysiological profiles of these diseases are disparate, involving the aggregation of different proteins, affecting distinctive cell types or tissues and having very different progression rates, they also share common structural, biochemical and biological features suggesting that amyloids might also have similar modes of interaction with cellular components(*8*). Although amyloids of different proteins have been shown to interact with lipids(*40*), proteins(*41*) and nucleic acids(*42*), it is currently unclear which of these interactions are relevant for disease. While some amyloid interactions are rather unspecific, e.g. with biological lipids(*43*) other amyloid interactions are highly specific(*20*). The most prominent of these is the self-interaction of amyloidogenic sequences during amyloid fibril formation which includes both amyloid nucleation and fiber elongation(*44, 45*). Proteome wide studies using amyloid prediction algorithms suggest that most proteins possess amyloidogenic sequence segments within their structure even though they do not form amyloid under normal conditions(*5, 6*). Given the sequence specificity of amyloid seeding this suggests that amyloid aggregation should be specifically inducible in non-amyloid associated proteins by exposing them to amyloidogenic peptides derived from their own sequence.

Here we demonstrate that aggregation of endogenously expressed VEGFR2 can be induced under physiological conditions by exposing it to vascin, a peptide consisting of a tandem repeat of an amyloidogenic sequence in its signal peptide. We find that vascin possesses all attributes of natural amyloids including cross-beta structure, the population of amyloid precursor aggregates, and the ability to reach the cytoplasmic compartment of cells, confirming that the signal peptide of VEGFR2 possesses a genuine amyloidogenic sequence. In addition we find that vascin is able to induce VEGFR2 aggregation by direct interaction with VEGFR2. As vascin is targeting the VEGFR2 signaling peptide, seeding of VEGFR2 aggregation is likely to be co-translational as suggested by ribosomal colocalization of vascin in the cytoplasm and the occurrence of partial VEGFR2 degradation along with its

aggregation. This results in VEGFR2 inactivation *in vitro* but also *in vivo* where it inhibits VEGFR2 dependent tumor growth upon intravascular administration. Both the aggregation as well as the inhibition of VEGFR2 appears to be specific. Indeed, scrambled vascin or the proline mutant do not interact with VEGFR2, nor does it provoke VEGFR2 aggregation or inhibition. In addition, whereas vascin suppresses cell surface presentation of VEGFR2, it does not affect trafficking of other receptors such as CD29 or EGFR. Finally, vascin-induced VEGFR2 aggregation is not inherently toxic as it does not affect the viability of VEGFR2 overexpressing HEK293 cells. Together these findings show that VEGFR2, a protein not associated with amyloid disease, can be specifically induced to aggregate in the presence of specific amyloid seeds that are derived from its own sequence.

There may be multiple reasons why large scale amyloidosis is not observed under natural conditions despite the likely prevalence of potentially amyloidogenic sequences in many proteins. First, most amyloidogenic sequences are buried in globular protein domains, which is probably the main protective factor against amyloidosis(*46*). Moreover, most misfolded proteins will be actively degraded in the cell before they have the opportunity to aggregate(*47*). Secondly, even in unfolded or intrinsically disordered proteins most amyloidogenic sequences are generally still sufficiently protected from aggregation by structural mechanisms such as gatekeeping(*48*) (i.e. the inhibition of aggregation by charged residues adjacent to the amyloidogenic segment) and entropic bristles(*49*) (i.e. unstructured protein segments that entropically prevent the association of amyloidogenic sequences). Finally interaction with molecular chaperones will also contribute to the inhibition of aggregation(*50*). The reason why vascin can overcome these potential protective mechanisms is not yet clear but might reside in its design: vascin comprises a tandem repeat of an amyloidogenic sequence, which exacerbates the aggregation propensity of this sequence and leads to the formation of soluble and stable oligomeric aggregates, and these are likely to provide efficient sites for seeding. Incidentally, yeast prions often consist of peptide sequence repeats(*32*) and the stability of soluble oligomers consisting of tandem peptide repeats recently allowed their structure solvation by X-ray crystallography(*29*).

The toxic gain-of-function observed in many amyloid-associated diseases remains poorly explained. This is mainly due to the impossibility to relate loss-of-

function effects to the aggregation process of a given protein. Indeed for many amyloid proteins, especially in neurodegeneration, the functional role of the affected protein is often complex and not entirely understood(*25, 26*), which makes it difficult to unequivocally identify loss-of-function effects. In addition the interactions of amyloid with cellular components in disease is also not clarified so that again gain-of-toxic function is not directly tractable at the molecular level. The availability of our artificial amyloid model provides an opportunity to study the relationship between amyloid toxicity and specific protein loss-of-function. Indeed while recapitulating essential amyloid features our model also allows to monitor the effect of amyloidosis on a functionally well-characterized protein. Moreover, the use of a VEGFR2 fragment allows assessing amyloid toxicity independently of VEGFR2 function.

Our results demonstrate that using this setup vascin does not display generic toxic properties but rather to the contrary. Vascin gain-of-function is specific (i.e. it is dependent on the presence of VEGFR2) but also conditional (i.e. VEGFR2 needs to be expressed in the cell but the cell also needs to be dependent on VEGFR2 for its survival/proliferation). Indeed in VEGFR2 dependent HUVECs vascin toxicity and VEGFR2 loss-of-function correlate in a dose-responsive manner whereas this is not the case in VEGFR2 expressing HEK293 cells. Together these results therefore illustrate how amyloid toxicity can result from a conjunction of protein specific and cell dependent protein loss-of-function. Whether lack of generalized toxicity is coupled to the availability of specific 'aggregation epitopes' during or after translation remains to be further explored. It is possible that only selected APRs, occuring in the right structural context, would be sensitive to co-aggregation. However, the results in other model systems, such as plants (*31*) and bacteria (*30*), suggest that this not the most likely scenario, but that the selectivity comes from the seqeunce specificity of the amyloid interaction (*20, 51*). Further studies are needed to clarify this point.

Materials and Methods

Bioinformatics

We used the TANGO algorithm for all APR identifications in this manuscript. We used a cutoff on the TANGO score of 5 per residue since this gives a Mathews Correlation Coefficient between prediction and experiment of 0.92(*28*). The settings of TANGO were Temperature = 298K, pH = 7.5, Ionic Strength = 0.10 M.

Peptides

Peptides were synthesized in-house using an Intavis Multipep RSi synthesis robot. Raw peptides were stored as dry ether precipitates at -20 °C prior to use. Purified peptides where lyophilized and closed under nitrogen atmosphere and stored at -20 °C prior to use. Stock solutions of each peptide were prepared fresh in 1% w/v ammonium bicarbonate in MiliQ water, filtered through 0.22 μm regenerated cellulose filter (Whatman, USA) and used immediately. The concentration of the peptides stocks was determined by absorbance at 280 nm using the calculated molar extinction coefficient $\varepsilon = 11380$ $M^{-1}cm^{-1}$.

Cell lines and media

HUVEC cells (Lonza) were grown in EGM2 complete medium (Lonza) in flasks pre-coated with 0.1% gelatin. The cells were never allowed to grow confluent and were only used for experiments between passage p3 and p9. U2-Os and HEK293 cells were maintained in DMEM medium, supplemented with 10% FBS, 1 mM sodium pyruvate, non-essential amino acids and antibiotics (penicillin/streptomycin). Lipofectamine 2000 (Life Technologies) was used to transiently transfect HEK293 and U2OS cells with an expression vector for VEGFR2 (pCDNA3) generating the cell lines HEK293^{VEGFR2} and U2OS^{VEGFR2}. All peptide treatments were done in DMEM/F12 medium without additives. Toxicity of the peptide treatments was evaluated using the CellTiter-Blue Cell Viability Assay according to the instructions of the manufacturer (Promega, USA).

Quantification of growth factor signaling

HUVEC, HEK293, U2OS, HEK293^{VEGFR2} and U2OS^{VEGFR2} cells were treated with peptide overnight. The next day cells were stimulated with 25 ng/ml recombinant mouse-

VEGF (493-MV, R&D Systems) or recombinant human-EGF (236-EG, R&D Systems) for exactly 5 min at 37°C. Cells were washed twice with ice cold PBS and lysed in RIPA lysis buffer (ThermoFisher Scientific) supplement with Complete protease inhibitor (Roche) and PhosSTOP phosphatase inhibitor (Roche). Quantification of VEGFR2 autophosphorylation and ERK phosphorylation was performed by electrochemiluminescence ELISA using the following kits according to the manufacturer's recommended protocol: Phospho-VEGFR-2(Tyr1054) (K151DJD, Meso Scale Discovery) and Phospho(Thr202/Tyr204; Thr185/Tyr187)/Total ERK1/2 (K15107D, Meso Scale Discovery).

X-ray fiber diffraction
X-ray fiber diffraction samples were made by allowing a droplet of the stock fibril solution to dry between two wax tipped capillary tubes. X-ray diffraction data was collected using a Rigaku rotating anode (CuKa) with Saturn CCD detector with exposure times of 30-60 seconds and specimen to detector distance of 50 or 100 mm. Reflections were measured using CLEARER (*52*).

In vivo experiments
All animal procedures were approved by the local animal ethical committee. Female C57BL/6 mice, 8 weeks of age, were purchased from Janvier (France). The B16.F10 melanoma cell line was obtained from the American Type Culture Collection (ATCC) and maintained in Dulbecco's Modified Eagle's Medium (DMEM) supplemented with 10% fetal bovine serum. B16 cells ($5x10^5$ cells/mouse) were implanted subcutaneously in the right dorsal flank of C57BL/6 mice. Starting from 3 days after tumor implantation, mice were randomized in three groups and treated daily by intravenous delivery of vascin or scrambled vascin (10mg/kg), or by oral delivery of PTK787 (75mg/kg). Tumors growth was monitored by caliper measurement every 2–3 days starting from 10 days after tumor injection. The experiment had 10 animals per group at onset, except the PTK group, which had five.

Transmission Electron Microscopy (TEM)
For each sample 7 μL aliquots of peptide solution were adsorbed for 1 minute to formvar film coated copper grids of 400-mesh (Agar Scientific Ltd., England) that

were first glow discharged to improve adsorption. After sample adsorption grids were washed by contact with 5 drops of ultrapure water and stained by contact with one drop of uranyl acetate (2% w/v in MiliQ water) for 45 sec. The grids were examined using a JEM-2100 transmission electron microscope (Jeol, Japan) at 80 keV.

Biophysical characterization

Dynamic light scattering (DLS) measurements were made at room temperature with a DynaPro DLS plate reader instrument (Wyatt, Santa Barbara, CA, USA) equipped with a 830-nm laser source. Samples (100 μL 300 μM peptide stock) were placed into a flat-bottom 96-well microclear plate (Greiner, Germany). The autocorrelation of scattered light intensity at a 90° angle was recorded for 10 s and averaged over 40 recordings to obtain a single data point. The Wyatt Dynamics software was used to calculate the hydrodynamic radius by assuming linear polymer particles. Attenuated Total Reflection Fourier Transform Infrared Spectroscopy (ATR FTIR) was performed using a Bruker Tensor 27 infrared spectrophotometer (Bruker, Germany) equipped with a Bio-ATR II accessory (Harrick Scientific Products, USA). Spectra were recorded in the range of 900 –3500 cm^{-1} at a spectral resolution of 2 cm^{-1} by accumulating 256 data acquisitions. The spectrophotometer was continuously purged with dried air. Spectra were corrected for atmospheric water vapor interference, baseline-subtracted, and vector normalized in the amide II area (1500 to 1600 cm-1) as implemented in OPUS software (Bruker). Tinctorial analysis was performed by incubating vascin or its scrambled version at the concentration indicated on each figure with 20 μM ThT, 20 μM ANS or 0.3 μM h-HTAA and fluorescence emission was recorded in a PolarStar Optima plate reader (BMG labtech, Germany) equipped with 360 nm and 490 nm excitation filters and 460 nm and 520 nm emission filters. All filters had 10 nm band-pass. Emission fluorescence spectra of h-HTAA bound to vascin or scrambled vascin were recorded in a FlexStation 3 (Molecular Devices, USA) at the same concentration of peptide and fluorophore listed above, with excitation at 480 nm and emission recorded between 490 nm and 620 nm using 10 nm band-pass.

Statistics

Statistical analysis was performed using Prism, Origin or R. Unpaired student's t-test and anova were used to determine significant differences between samples unless otherwise indicated. Significance levels: * for $p < 0.05$, ** for $p < 0.01$, *** for $p < 0.001$.

Supplementary Content

22. References exclusively cited in the supplementary information: (*53*) (*54*) (*52*) (*55*) (*56-58*) (*59-65*) (*66*) (*67*)

References

1. K. Dudgeon, K. Famm, D. Christ, Sequence determinants of protein aggregation in human VH domains. *Protein Engineering Design & Selection* **22**, 217-220 (2009).
2. S. Ventura *et al.*, Short amino acid stretches can mediate amyloid formation in globular proteins: the Src homology 3 (SH3) case. *Proc Natl Acad Sci U S A* **101**, 7258-7263 (2004).
3. O. S. Makin, L. C. Serpell, Structures for amyloid fibrils. *Febs J* **272**, 5950-5961 (2005).
4. D. Eisenberg *et al.*, Amyloid and prion structures. *Faseb Journal* **23**, (2009).
5. F. Rousseau, L. Serrano, J. W. H. Schymkowitz, How evolutionary pressure against protein aggregation shaped chaperone specificity. *Journal of Molecular Biology* **355**, 1037-1047 (2006).
6. L. Goldschmidt, P. K. Teng, R. Riek, D. Eisenberg, Identifying the amylome, proteins capable of forming amyloid-like fibrils. *Proceedings of the National Academy of Sciences of the United States of America* **107**, 3487-3492 (2010).
7. F. Chiti, C. M. Dobson, Protein misfolding, functional amyloid, and human disease. *Annual Review of Biochemistry* **75**, 333-366 (2006).
8. D. Eisenberg, M. Jucker, The amyloid state of proteins in human diseases. *Cell* **148**, 1188-1203 (2012).
9. K. E. Marshall, R. Marchante, W. F. Xue, L. C. Serpell, The relationship between amyloid structure and cytotoxicity. *Prion* **8**, 192-196 (2014).
10. M. R. Krebs *et al.*, Formation and seeding of amyloid fibrils from wild-type hen lysozyme and a peptide fragment from the beta-domain. *J Mol Biol* **300**, 541-549 (2000).
11. J. T. Jarrett, E. P. Berger, P. T. Lansbury, Jr., The carboxy terminus of the beta amyloid protein is critical for the seeding of amyloid formation: implications for the pathogenesis of Alzheimer's disease. *Biochemistry* **32**, 4693-4697 (1993).
12. W. Li *et al.*, Aggregation promoting C-terminal truncation of alpha-synuclein is a normal cellular process and is enhanced by the familial Parkinson's disease-linked mutations. *Proc Natl Acad Sci U S A* **102**, 2162-2167 (2005).
13. Y. Wang, S. Garg, E. M. Mandelkow, E. Mandelkow, Proteolytic processing of tau. *Biochem Soc Trans* **38**, 955-961 (2010).
14. S. Nystrom, P. Hammarstrom, Generic amyloidogenicity of mammalian prion proteins from species susceptible and resistant to prions. *Sci Rep* **5**, 10101 (2015).
15. R. S. Rajan, M. E. Illing, N. F. Bence, R. R. Kopito, Specificity in intracellular protein aggregation and inclusion body formation. *Proc Natl Acad Sci U S A* **98**, 13060-13065 (2001).
16. M. R. Krebs, L. A. Morozova-Roche, K. Daniel, C. V. Robinson, C. M. Dobson, Observation of sequence specificity in the seeding of protein amyloid fibrils. *Protein Sci* **13**, 1933-1938 (2004).
17. J. Xu *et al.*, Gain of function of mutant p53 by coaggregation with multiple tumor suppressors. *Nat Chem Biol* **7**, 285-295 (2011).
18. K. Ono, R. Takahashi, T. Ikeda, M. Yamada, Cross-seeding effects of amyloid beta-protein and alpha-synuclein. *J Neurochem* **122**, 883-890 (2012).

19. M. E. Oskarsson *et al.*, In vivo seeding and cross-seeding of localized amyloidosis: a molecular link between type 2 diabetes and Alzheimer disease. *Am J Pathol* **185**, 834-846 (2015).
20. A. Ganesan *et al.*, Selectivity of aggregation-determining interactions. *J Mol Biol* **427**, 236-247 (2015).
21. W. Surmacz-Chwedoruk, V. Babenko, W. Dzwolak, Master and slave relationship between two types of self-propagating insulin amyloid fibrils. *J Phys Chem B* **118**, 13582-13589 (2014).
22. K. H. Ashe, A. Aguzzi, Prions, prionoids and pathogenic proteins in Alzheimer disease. *Prion* **7**, (2012).
23. K. F. Winklhofer, J. Tatzelt, C. Haass, The two faces of protein misfolding: gain- and loss-of-function in neurodegenerative diseases. *EMBO J* **27**, 336-349 (2008).
24. M. Jucker, L. C. Walker, Self-propagation of pathogenic protein aggregates in neurodegenerative diseases. *Nature* **501**, 45-51 (2013).
25. H. A. Pearson, C. Peers, Physiological roles for amyloid beta peptides. *J Physiol* **575**, 5-10 (2006).
26. J. T. Bendor, T. P. Logan, R. H. Edwards, The function of alpha-synuclein. *Neuron* **79**, 1044-1066 (2013).
27. I. Benilova, E. Karran, B. De Strooper, The toxic A beta oligomer and Alzheimer's disease: an emperor in need of clothes. *Nature Neuroscience* **15**, 349-357 (2012).
28. A. M. Fernandez-Escamilla, F. Rousseau, J. Schymkowitz, L. Serrano, Prediction of sequence-dependent and mutational effects on the aggregation of peptides and proteins. *Nat Biotechnol* **22**, 1302-1306 (2004).
29. A. Laganowsky *et al.*, Atomic view of a toxic amyloid small oligomer. *Science* **335**, 1228-1231 (2012).
30. N. G. Bednarska *et al.*, Protein aggregation as an antibiotic design strategy. *Mol Microbiol*, (2015).
31. C. Betti *et al.*, Sequence-Specific Protein Aggregation Generates Defined Protein Knockdowns in Plants. *Plant physiology* **171**, 773-787 (2016).
32. E. D. Ross, A. Minton, R. B. Wickner, Prion domains: sequences, structures and interactions. *Nat Cell Biol* **7**, 1039-1044 (2005).
33. R. Sabate, F. Rousseau, J. Schymkowitz, S. Ventura, What makes a protein sequence a prion? *PLoS Comput Biol* **11**, e1004013 (2015).
34. T. Klingstedt *et al.*, Synthesis of a library of oligothiophenes and their utilization as fluorescent ligands for spectral assignment of protein aggregates. *Organic & biomolecular chemistry* **9**, 8356-8370 (2011).
35. L. M. Young *et al.*, Screening and classifying small-molecule inhibitors of amyloid formation using ion mobility spectrometry-mass spectrometry. *Nat Chem* **7**, 73-81 (2015).
36. S. Campioni *et al.*, A causative link between the structure of aberrant protein oligomers and their toxicity. *Nat Chem Biol* **6**, 140-147 (2010).
37. D. Pinotsi *et al.*, Direct observation of heterogeneous amyloid fibril growth kinetics via two-color super-resolution microscopy. *Nano Lett* **14**, 339-345 (2014).
38. J. M. Wood *et al.*, PTK787/ZK 222584, a novel and potent inhibitor of vascular endothelial growth factor receptor tyrosine kinases, impairs vascular

endothelial growth factor-induced responses and tumor growth after oral administration. *Cancer Res* **60**, 2178-2189 (2000).

39. R. Radde *et al.*, Abeta42-driven cerebral amyloidosis in transgenic mice reveals early and robust pathology. *EMBO Rep* **7**, 940-946 (2006).

40. H. A. Lashuel, D. Hartley, B. M. Petre, T. Walz, P. T. Lansbury, Jr., Neurodegenerative disease: amyloid pores from pathogenic mutations. *Nature* **418**, 291 (2002).

41. H. Olzscha *et al.*, Amyloid-like aggregates sequester numerous metastable proteins with essential cellular functions. *Cell* **144**, 67-78 (2011).

42. D. Cirillo *et al.*, Neurodegenerative diseases: quantitative predictions of protein-RNA interactions. *RNA* **19**, 129-140 (2013).

43. G. P. Gorbenko, P. K. Kinnunen, The role of lipid-protein interactions in amyloid-type protein fibril formation. *Chem Phys Lipids* **141**, 72-82 (2006).

44. R. Wetzel, Kinetics and thermodynamics of amyloid fibril assembly. *Acc Chem Res* **39**, 671-679 (2006).

45. S. I. Cohen *et al.*, Proliferation of amyloid-beta42 aggregates occurs through a secondary nucleation mechanism. *Proc Natl Acad Sci U S A* **110**, 9758-9763 (2013).

46. F. Chiti, C. M. Dobson, Amyloid formation by globular proteins under native conditions. *Nat Chem Biol* **5**, 15-22 (2009).

47. G. De Baets *et al.*, An evolutionary trade-off between protein turnover rate and protein aggregation favors a higher aggregation propensity in fast degrading proteins. *PLoS Comput Biol* **7**, e1002090 (2011).

48. G. De Baets, J. Durme, F. Rousseau, J. Schymkowitz, A Genome-Wide Sequence-Structure Analysis Suggests Aggregation Gatekeepers Constitute an Evolutionary Constrained Functional Class. *Journal of Molecular Biology* **426**, 2405-2412 (2014).

49. A. A. Santner *et al.*, Sweeping away protein aggregation with entropic bristles: intrinsically disordered protein fusions enhance soluble expression. *Biochemistry* **51**, 7250-7262 (2012).

50. R. I. Morimoto, The heat shock response: systems biology of proteotoxic stress in aging and disease. *Cold Spring Harbor symposia on quantitative biology* **76**, 91-99 (2011).

51. J. R. Couceiro *et al.*, Sequence-dependent Internalization of Aggregating Peptides. *J Biol Chem* **290**, 242-258 (2015).

52. S. Zibaee, O. S. Makin, M. Goedert, L. C. Serpell, A simple algorithm locates beta-strands in the amyloid fibril core of alpha-synuclein, Abeta, and tau using the amino acid sequence alone. *Protein Sci* **16**, 906-918 (2007).

53. S. Wolter *et al.*, rapidSTORM: accurate, fast open-source software for localization microscopy. *Nat Methods* **9**, 1040-1041 (2012).

54. P. Annibale, M. Scarselli, M. Greco, A. Radenovic, Identification of the factors affecting co-localization precision for quantitative multicolor localization microscopy. *Optical Nanoscopy* **1**, 1-13 (2012).

55. Y. Shi, P. Kirwan, F. J. Livesey, Directed differentiation of human pluripotent stem cells to cerebral cortex neurons and neural networks. *Nat Protoc* **7**, 1836-1846 (2012).

56. G. Morawietz *et al.*, Revised guides for organ sampling and trimming in rats and mice--Part 3. A joint publication of the RITA and NACAD groups. *Exp Toxicol Pathol* **55**, 433-449 (2004).

57.   B. Kittel *et al.*, Revised guides for organ sampling and trimming in rats and mice--Part 2. A joint publication of the RITA and NACAD groups. *Exp Toxicol Pathol* **55**, 413-431 (2004).
58.   C. Ruehl-Fehlert *et al.*, Revised guides for organ sampling and trimming in rats and mice--part 1. *Exp Toxicol Pathol* **55**, 91-106 (2003).
59.   D. Dixon *et al.*, Nonproliferative and proliferative lesions of the rat and mouse female reproductive system. *J Toxicol Pathol* **27**, 1S-107S (2014).
60.   P. Greaves *et al.*, Proliferative and non-proliferative lesions of the rat and mouse soft tissue, skeletal muscle and mesothelium. *J Toxicol Pathol* **26**, 1S-26S (2013).
61.   W. Kaufmann *et al.*, Proliferative and nonproliferative lesions of the rat and mouse central and peripheral nervous systems. *Toxicol Pathol* **40**, 87S-157S (2012).
62.   B. Thoolen *et al.*, Proliferative and nonproliferative lesions of the rat and mouse hepatobiliary system. *Toxicol Pathol* **38**, 5S-81S (2010).
63.   K. S. Frazier *et al.*, Proliferative and nonproliferative lesions of the rat and mouse urinary system. *Toxicol Pathol* **40**, 14S-86S (2012).
64.   L. Mecklenburg *et al.*, Proliferative and non-proliferative lesions of the rat and mouse integument. *J Toxicol Pathol* **26**, 27S-57S (2013).
65.   T. Nolte *et al.*, Nonproliferative and Proliferative Lesions of the Gastrointestinal Tract, Pancreas and Salivary Glands of the Rat and Mouse. *J Toxicol Pathol* **29**, 1S-125S (2016).
66.   S. Nystrom *et al.*, Multiple substitutions of methionine 129 in human prion protein reveal its importance in the amyloid fibrillation pathway. *J Biol Chem* **287**, 25975-25984 (2012).
67.   S. Raitano *et al.*, Restoration of progranulin expression rescues cortical neuron generation in an induced pluripotent stem cell model of frontotemporal dementia. *Stem Cell Reports* **4**, 16-24 (2015).

Acknowledgements

Figure Legends

Figure 1 – Biophysical characterization of the amyloids formed by vascin. (A-D) Transmission Electron Microscopy image of 300 μM vascin in 1% (w/v) NH_4CO_3 after 24h incubation at room temperature and negatively stained with 2% (w/v) uranyl acetate. **(E)** Tinctorial analysis of fibrils of 300 μM vascin in 1% (w/v) NH_4CO_3 after 18h incubation at room temperature. The bars show the mean of 3 measurements and the error bars show the standard deviation. **(F)** Fiber x-ray diffraction pattern of fibrils formed in 300 μM vascin in 1% (w/v) NH_4CO_3. **(G)** ESI–IMS–MS Driftscope plot of the vascin monomer (1) through to the heptamer (7) present two minutes after diluting the monomer to a final peptide concentration of 100 μM in in 1% (w/v) NH_4CO_3. ESI–IMS–MS Driftscope plots show the IMS drift time versus mass/charge (*m/z*) versus intensity (z, square-root scale). **(H)** Histogram of size distribution of particles calculated from the DLS data recorded during vascin aggregation using a linear polymer as particle model. **(E)** FT-IR Spectrum of 300 μM vascin in 1% (w/v)

NH_4CO_3 at t= 5 min (red) and t= 24h (blue). (J) Time progression of the intensity of the absorbtion peak in the FT-IR spectrum in panel E around 1622 cm^{-1}.

Figure 2 – Vascin directly interacts with VEGFR2 in cells (A) Cellular distribution CF-vascin^{K11} (green) at 1 μM in HUVEC cells. **(B)** Overlay between the fluorescence of Alexa647-labeled vascin^{K11} (20 μM, red) and the amyloid specific dye pFTAA (15 μM, green). Overlap is shown as yellow colouring. **(C)** Equivalent image as B for the proline mutant of vascin. **(D)** HUVEC cells treated for 4 hours with CF-vascin^{K11} (2.5 μM, green) and co-immunostained for the ER-specific marker calnexin (red). **(E)** HUVEC cells treated for 4 hours with CF-vascin^{K11} (5.0 μM, green) and co-immunostained for the ribosomal protein S6 (red). **(F)** Proximity ligation (Duo-Link) between CF-vascin^{K11} at 5.0 μM and VEGFR2 performed in HUVEC cells treated for 4 hours with peptide. For panels A, D, E and F the nuclei are stained with DAPI in blue. **(G)** Quantification of the Duo-Link signal by high content microscopy of HUVEC cells treated with vascin as depicted in (E). For each condition about 700 cells were analyzed and the average fluorescence intensity per cell is shown. The box shows the interquartile range of the 25 to 75 percentile. The line in the middle of the box indicates the median and the lines extending from the box indicate the 99% limits of the distribution. Outliers are shown as circles. **(H)** dSTORM image of HUVEC cells treated for 4 hours with 0.5 μM Alexa647-labeled vascin^{K11} (purple) and co-immunostained for VEGFR2 (green). Scale bar is 1 μm. **(I)** Magnification of image in G where arrowheads indicate the interaction of vascin and VEGFR2. Scale bar is 1 μm.

Figure 3 – Vascin knocks down VEGFR2 activity. (A) Western blot analysis for VEGFR2 co-immunoprecipitation in HUVEC cells treated for 4 hours with 20 μM biotin-PEG labeled vascin. **(B)** Western blot analysis of the partitioning of VEGFR2 between the soluble and insoluble fraction of HUVEC cells treated with 20 μM vascin. **(C)** Western blot analysis of the SDS-gradient extraction of the soluble and insoluble fraction of HUVEC cells treated with 20 μM vascin. **(D)** Dose-response curve of the effect of 2.5-100 μM vascin on VEGF stimulation of VEGFR2 autophosphorylation in HUVEC cells. The plot shows the mean of three measurements and the standard deviation. Curve fitting was performed **(E)** Dose-response curve of the effect of 2.5-

100 µM vascin on VEGF stimulation of ERK phosphorylation in HUVEC cells. The data is shown as the mean of four replicates and the standard deviation. **(F)** VEGFR2 autophosphorylation and ERK phosphorylation in HUVEC cells treat with 20 µM vascin, human vascin (h.vascin), scrambled vascin and proline mutant vascin (Pro). The bars show the mean of four measurements and the error bars show the standard deviation. **(G)** Quantification by Fluorescence Activated Cell Sorting (FACS) of the fraction of 1cells that display VEGFR2 and CD29 on the cell surface upon treatment with vascin or scrambled vascin at 20 µM. Per condition 10.000 cells were analysed. The bars show the mean of three measurements and the error bars show the standard deviation. The star indicates a p-value <0.05 calculated by student-t test compared to the non-treated condition. **(H)** Quantification of ERK phosphorylation level as determined by MSD assay upon EGF stimulation of HeLa cells treated with 20 µM vascin or its scrambled version. The data is shown as the mean of four replicates and the standard deviation. **(I)** Lag phase of the aggregation kinetics of the Alzheimer β-peptide 1-40 (Aβ1–40) observed with Thioflavin T fluorescence in the presence of 1% molar fraction of homotypic seeds (self seed), or the equivalent amount of seeds of vascin, human vascin, scrambled vascin or the proline mutant vascin. **(J)** Equivalent experiment to panel I for the human Prion protein (HuPrP23-231). All aggregation kinetics experiments were run in 6 replicates and the bars show the mean value, with error bars showing the standard deviation. The statistically significant differences were identified using the Student t-test.

Figure 4 – In vivo effect of Vascin and cell-type dependent cytotoxicity. (A) Tumor growth curves of subcutaneously inject B6 melanoma cells in C57BL6 mice treated with daily intravenous injections of 10 mg/kg biotin-PEG vascin or its scrambled control. As a positive control we used the inhibitor of the VEGFR2 tyrosine kinase activity PTK787. The experiment had 10 animals per group, except the PTK group, which had five. The average and standard error of the mean are shown. Statistically significant differences were identified using anova and Tukey multiple comparison testing. **(B-H)** Dose dependent toxicity of vascin or its scrambled control tested from 2.5 µM – 100 µM by the CellTiter-Blue assay on **(B)** HUVEC cells, **(C)** HEK293 cells, **(D)** U2OS cells, **(E)** HEK293 cells transiently overexpressing VEGFR2, **(F)** U2OS cells transiently overexpressing VEGFR2, **(G)** Cortical primary neuron cells
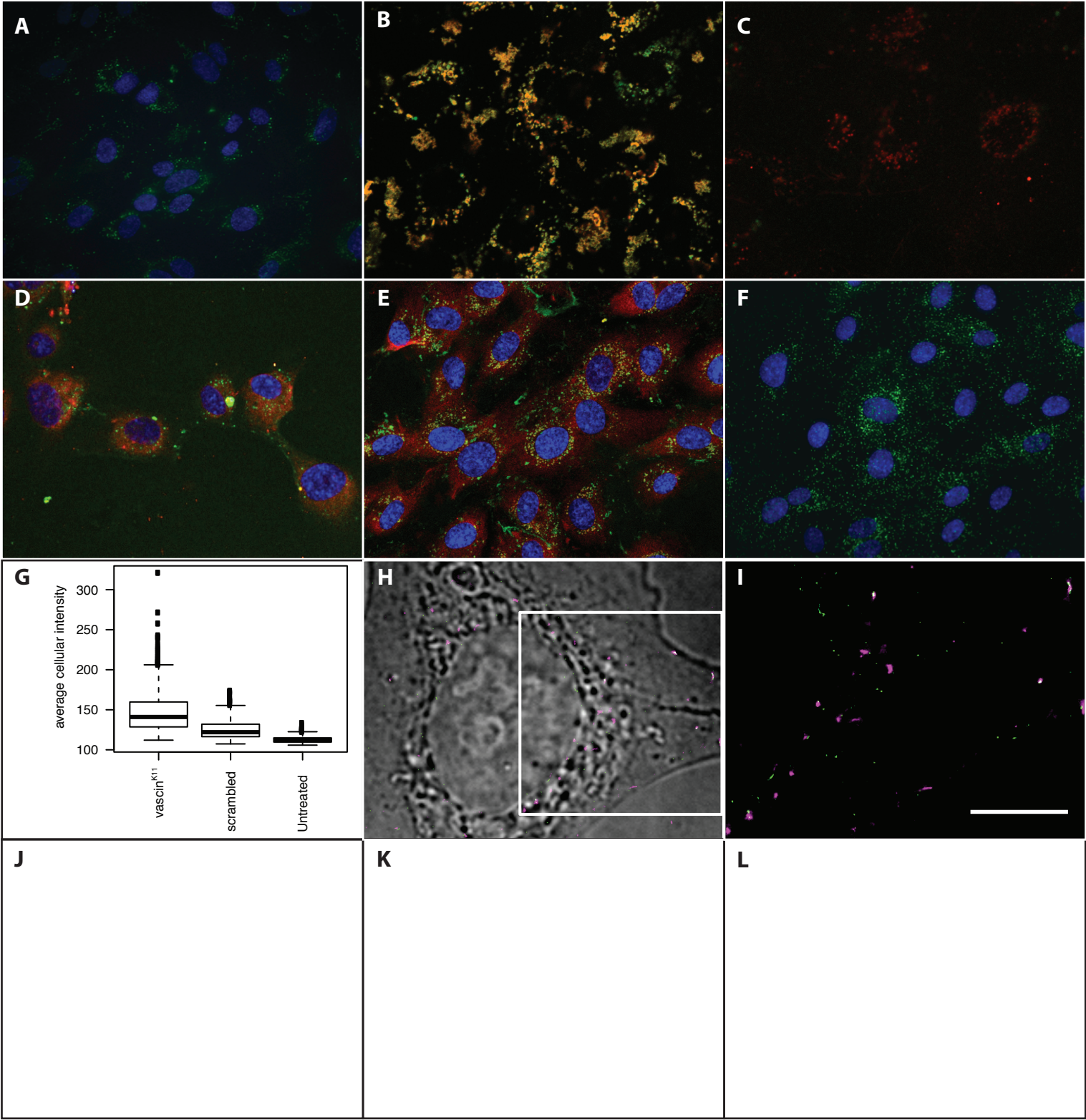
from mouse and **(H)** cortical neuronal progeny obtained from human induced pluripotent stem cells (iPSCs) after a neuronal differentiation protocol. All toxicity data is shown as the mean of five measurements with standard deviations, except the iPSC data which were 48 replicates. Statistically significant differences were identified using anova and Tukey multiple comparison testing.
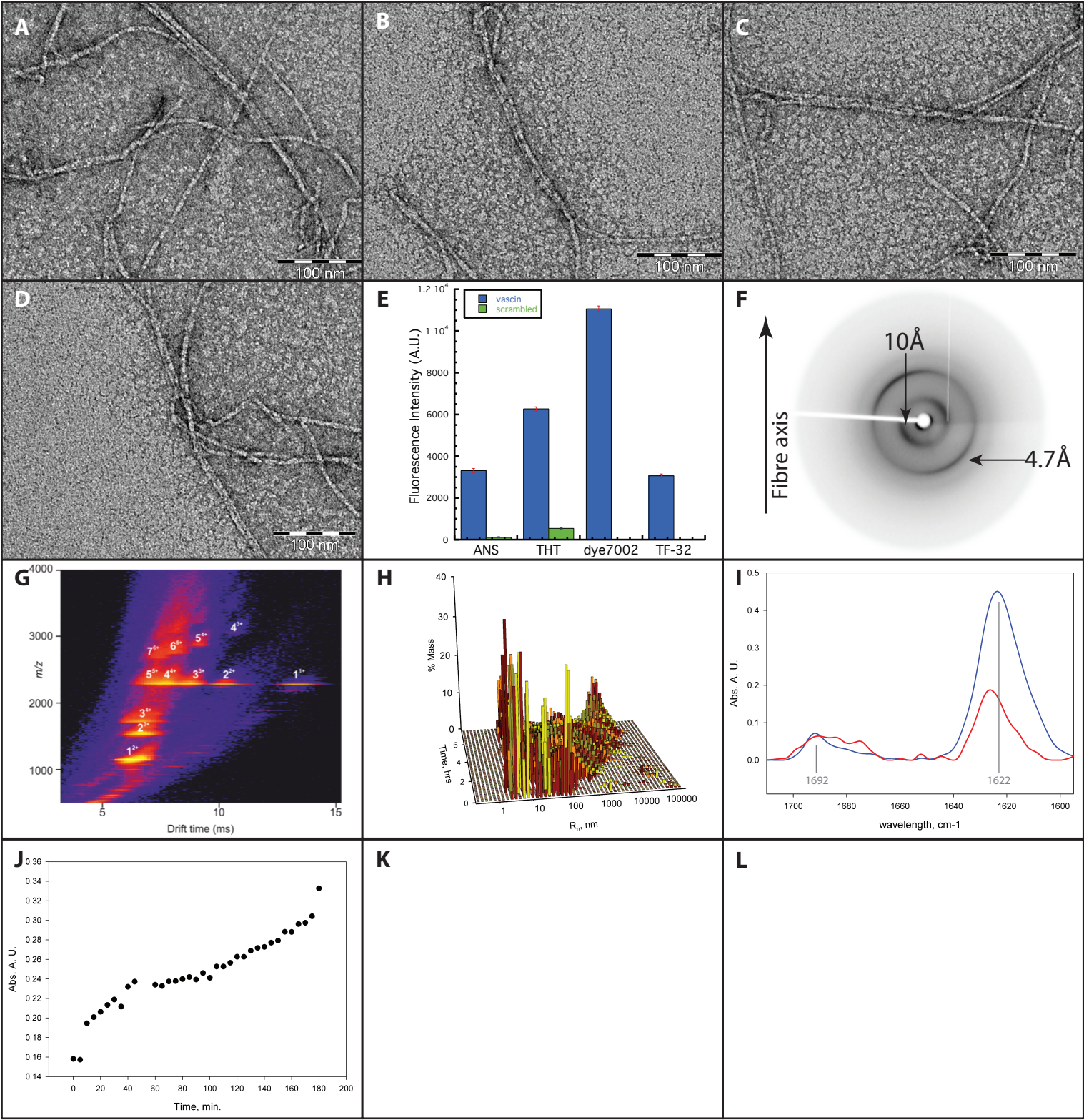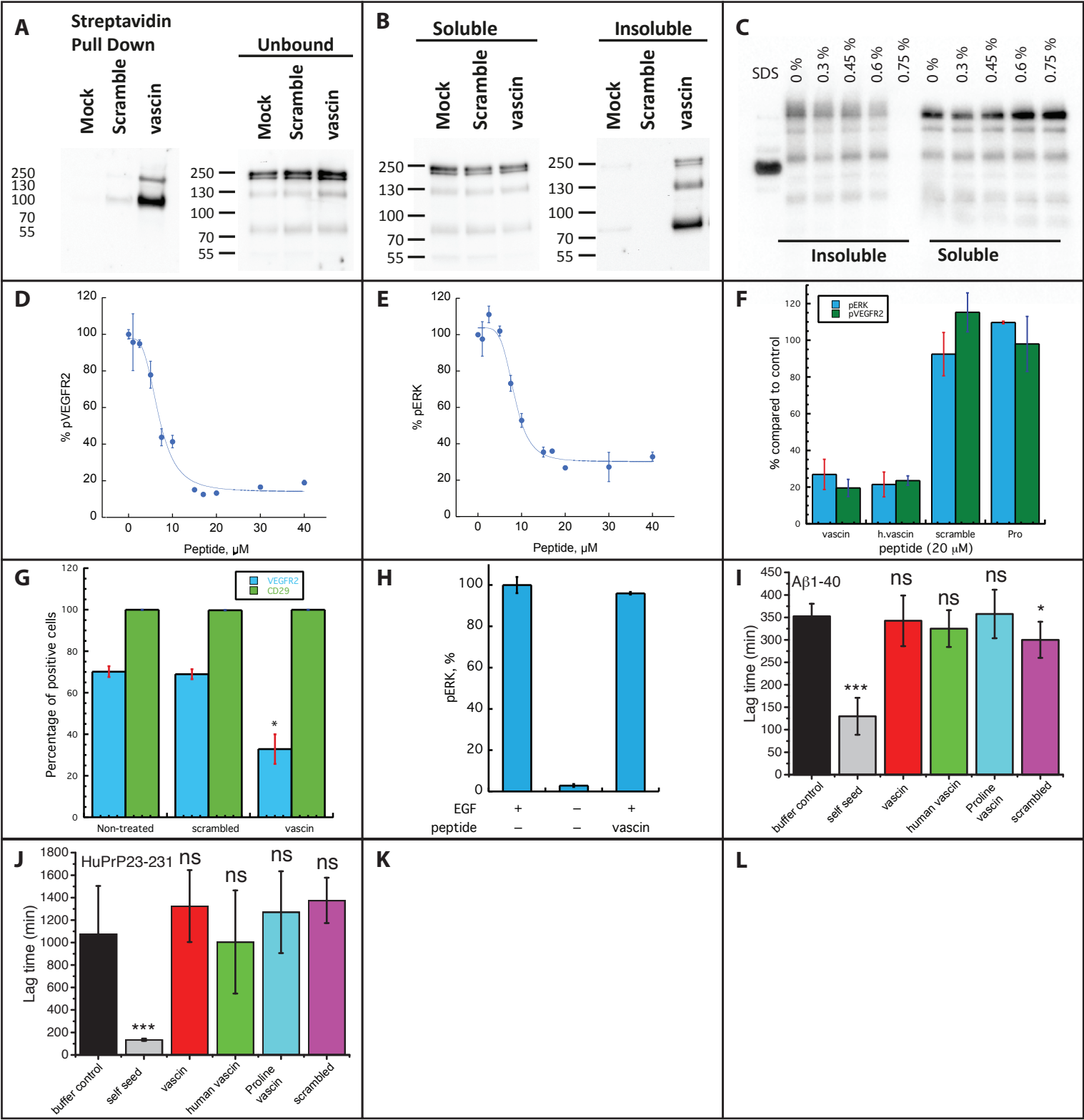
Gallardo et al, Figure 2

Gallardo et al, Figure 4